Graphitic carbon nitride based composite materials toward Synthesis and Photocatalytic Properties: Review

Lei Zhu *

Key Laboratory for Advanced Technology in Environmental Protection of Jiangsu Province, Yancheng Institute of Technology, Yancheng, 224051, P.R. China

Abstract: The utilization of solar energy with photocatalytic technology has been considered a good solution to alleviate environmental pollution and energy shortage. Graphitic carbon nitride ($g\text{-}C_3N_4$), a conjugated polymer semiconductor, has drawn increasing attention in environmental photocatalysis over the past decade, owing to its highly chemical stability, low cost and suitable electronic structure with a mild energy gap (~ 2.7 eV). The modification of $g\text{-}C_3N_4$ by coupling with other nanomaterials or forming unique nanostructures have been confirmed as valuable strategies. In this review, we give a comprehensive introduction about the recent developments in engineering $g\text{-}C_3N_4$ by constructing heterostructures which contains of $g\text{-}C_3N_4$/LDH, $g\text{-}C_3N_4$/2D semiconductor and $g\text{-}C_3N_4$/nanoscale photocatalysts. The performance and mechanisms of $g\text{-}C_3N_4$ based photocatalysts in hydrogen production, CO_2 reduction, and organic pollutant degradation are analyzed. Several enhanced photocatalytic mechanisms for these nanohybrids under visible light irradiation have been explicated in detail. This review is expected to provide basic insights into the design of $g\text{-}C_3N_4$ based composite photocatalysts and their applications in solar photocatalysis.

Keywords: $g\text{-}C_3N_4$, 2D semiconductor, LDH, nanoscale photocatalyst

1. Introduction

Graphic carbon nitride ($g\text{-}C_3N_4$) as an emerging star with two-dimensional characteristic structure, where tri-s-triazine units connected by amino groups in each layer, can be seen as a kind of nitrogen substituted graphene-like layered material [1]. Comparing with another carbon material of graphene, $g\text{-}C_3N_4$ own unique semiconductor properties, solid alkaline, and complexing ability [2,3]. Meanwhile graphitic carbon nitride ($g\text{-}C_3N_4$) is an organic semiconductor that has become one of the most widely studied and promising photocatalysts for treatment of water pollution. This is because $g\text{-}C_3N_4$ can absorb visible light and its bandgap is narrow (2.7 eV) [4,5]. Moreover, $g\text{-}C_3N_4$ offers the advantages of high thermal stability, nontoxicity, and low cost. On this basis, $g\text{-}C_3N_4$ is expected to have practical application to address energy shortages and environmental pollution [6,7]. It is known that the thickness, sizes, porous structure, and morphology

---

* Corresponding author: *E-mail: dream909@126.com*

of g-C_3N_4 can be controlled by using different experimental conditions. However, the specific surface area of g-C_3N_4 prepared via traditional methods is small, leading to low photocatalytic activity [8]. It thus becomes necessary to identify effective methods to increase the specific surface area and improve the photocatalytic efficiency of g-C_3N_4.
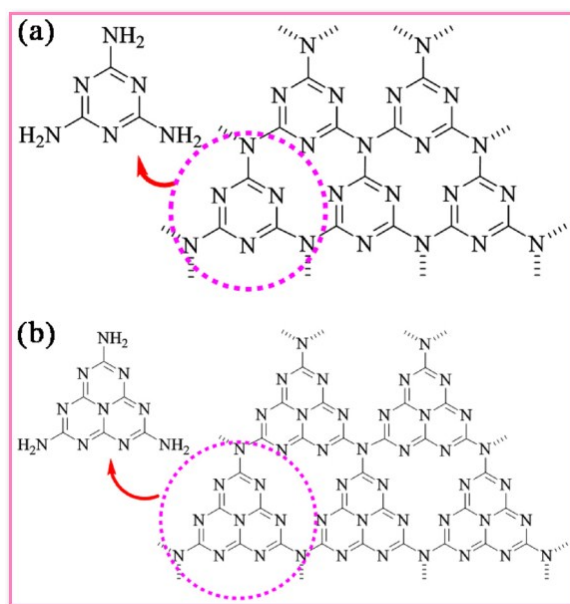
Schematic 1. (a) s-Triazine and (b) tri-s-triazine based structures of g-C_3N_4 [9].

Defect engineering (carbon vacancies or nitrogen vacancies) is considered as a simple and effective modification strategy for g-C_3N_4 by optimizing its electronic structure, optical characteristics and other physicochemical properties [10]. The slightly enhanced visible light absorption can be achieved by forming defect states between the forbidden bands of g-C_3N_4 and at the same time the separation efficiency of space charge can be significantly improved due to the weakened exciton effect. Moreover, the adsorption-activation ability of g-C_3N_4 for small molecules can also be improved by the charge localization effect of defects, resulting in the enhanced photocatalytic performance. However, most of the visible light and NIR light in the solar spectrum is not fully utilized. Hence, substantial attempts have been made to modify g-C_3N_4 for moderate electronic energy level and outstanding surface properties, including heteroatom doping, nanostructure design and incorporation with other materials [11,12]. Some noble metal modified g-C_3N_4 (Ag/g-C_3N_4 [13], Au/g-C_3N_4 [14]) and noble metal mediated g-C_3N_4-based indirect Z-scheme heterojunction (Au/$Cs_xZn_{1-x}S$/g-C_3N_4 [15], Au/BiOBr/g-C_3N_4 [16], Au/$BiVO_4$/g-C_3N_4 [17], $Ag_2Ta_4O_{11}$/Ag/g-C_3N_4 [18], Ag/MoS_2/g-C_3N_4 [19]) are designed and prepared to further improve the solar energy utilization, carriers' separation efficiency and redox ability of the photocatalytic system. However, considering the high prices of noble metals and the practical application of photocatalytic technology, direct Z-scheme hetero-structures with full-spectrum absorption need to be synthesized urgently.

With regarding to the fabrication of heterostructures, incorporating g-C_3N_4 with other 2D semiconductors, carbon-based materials or even metal oxide nanoparticles is an effective way to introduce the internal electric field or conducting media, conductive to inhibiting photoinduced charge-carrier recombination for the high photocatalytic performance [20–22]. Up to now, numerous interesting and significant findings on superior architectures of g-C_3N_4 and its hybrid composites have been reported, especially over the last few years. Some reports were focused on fabrication typical photocatalysts with different morphology followed by coupling with g-C_3N_4 for enhancement of its photocatalytic activity or photoelectrochemical activity. Li et.al reported that the g-C_3N_4/Bi_2MoO_6 heterojunction with a Bi_2MoO_6 content of 16.1 wt.% exhibited the highest photocatalytic activity, and its photocatalytic efficiency was more than three times those of pure g-C_3N_4 or Bi_2MoO_6 [23]. Liu et.al reported that high-efficiency direct Z-scheme g-C_3N_4/TiO_2 nanorod composites were fabricated for enhancing photocatalytic activity for RHB degradation. The 1.0% g-C_3N_4/TiO_2 nanorod exhibited the highest photocatalytic activity for RHB degradation, which was higher than those of the pure g-C_3N_4 and pure TiO_2 nanorods [24].

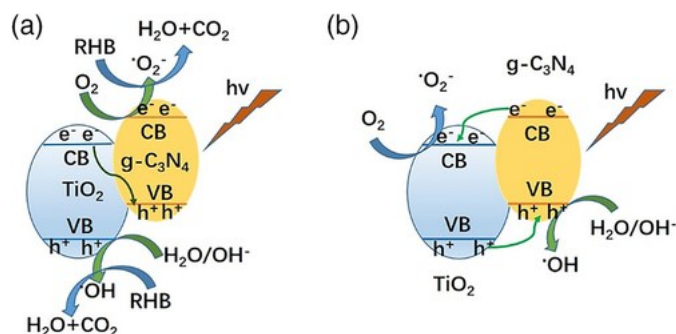**Fig. 1. Two proposed mechanisms for improving the photocatalytic performance of g-C_3N_4/ TiO_2 composites. (a) Z-scheme composite system, (b) heterojunction composite**

Although several excellent reviews have been presented concerning the effective modification of pristine g-C_3N_4 for wastewater treatment [25, 26], a systematical and comprehensive review on different nanostructure design is not yet reported and emphatically required to promote further developments for its targeted photocatalytic applications. At first, we will introduce basic degradation mechanisms of g-C_3N_4-based photocatalysis and the internal key steps. Subsequently, g-C_3N_4-based multicomponent systems are introduced, including LDH/g-C_3N_4 heterostructures, inorganic 2D semiconductor/g-C_3N_4 nanohybrids, g-C_3N_4/ based metal oxide complex hybrids and its focus on research about the development of visible-light-induced g-C_3N_4-based photocatalysts displayed.

2. Degradation mechanisms of single g-C_3N_4 and g-C_3N_4 based photocatalysis

The single g-C_3N_4 system, the photoexcited electrons in the conduction band (CB) tend to return to the valence band (VB), and the undesired recombination between photogenerated electrons and holes occurs, which is extremely unfavorable to the

photocatalytic reactions. When a semiconductor with a suitable band structure comes into intimate contact with g-C_3N_4, the spatial separation of photogenerated electron–hole pairs can be achieved through efficient charge transfer across the interface between the two semiconductors. Commonly, pristine g-C_3N_4 possesses a bandgap of about 2.7 eV, and the CB and VB positions are located at about -1.1 and +1.6 eV vs. normal hydrogen electrode (NHE), at pH 0, respectively [27]. As shown in Fig. 2, conventional g-C_3N_4-based type II heterojunction system is effective for separating photogenerated electron–hole pairs due to the staggered band structures of the component semiconductors. A suitable band structure is the key consideration in choosing the second semiconductor for constructing type II g-C_3N_4-based heterojunction.

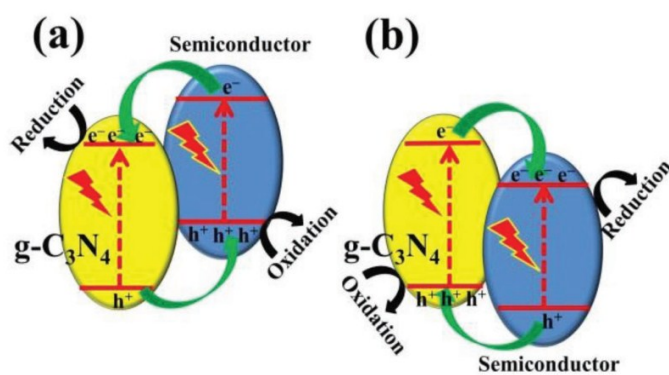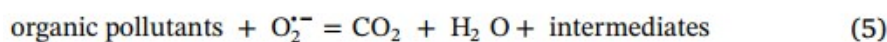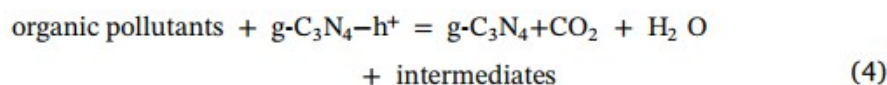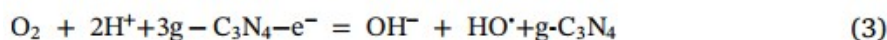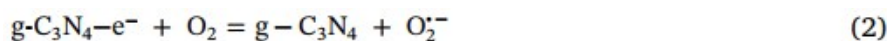**Fig.2. Conventional g-C_3N_4-based type II heterojunction system.**

During photocatalysis, g-C_3N_4 is directly excited by absorbing photons whose energies (hí) are larger than the energy gap (Eg) of g-C_3N_4, thus resulting in the generation of photoinduced electron-hole (e^- - h^+) pairs owing to the transfer of e^- from its valence band (VB) to conduction band (CB). The moderate Eg of g-C_3N_4 determines its good photoresponse to visible light. During photocatalysis, $O_2\%^-$ and h^+ play a vital role for g-C_3N_4 to degrade various organic contaminants into CO_2, H_2O and other small molecular products [28,29]. Moreover, the generation of reactive oxygen species from adsorbed O_2 by trapping e^- also contributes to restrain e^- - h^+ pairs recombination. The two photodegradation pathways for organic pollutants are schematically illustrated in Eqs. (4)–(5) and Fig. 3.
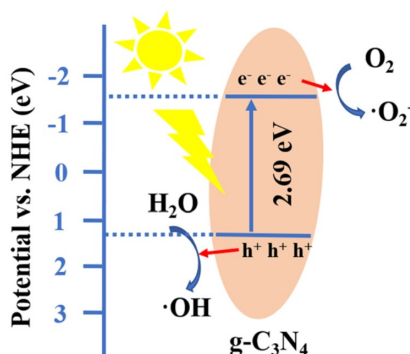
$$\text{g-}C_3N_4 - e^- + O_2 = \text{g} - C_3N_4 + O_2^{\cdot -} \tag{2}$$

$$O_2 + 2H^+ + 3\text{g} - C_3N_4 - e^- = OH^- + HO^{\cdot} + \text{g-}C_3N_4 \tag{3}$$

$$\text{organic pollutants} + \text{g-}C_3N_4 - h^+ = \text{g-}C_3N_4 + CO_2 + H_2O$$
$$+ \text{ intermediates} \tag{4}$$

$$\text{organic pollutants} + O_2^{\cdot -} = CO_2 + H_2O + \text{intermediates} \tag{5}$$

Fig. 3. Photocatalytic mechanism of single g-C_3N_4 system.

3. Graphitic carbon nitride based composite photocatalysts

3.1 g-C_3N_4/LDH photocatalysts

Though coupling LDH and g-C_3N_4 can increase the electron-hole separation, the charge carriers on some LDH/g-C_3N_4 photocatalysts are difficult to further transfer and participate in redox reactions [30]. Therefore, constructing LDH/g-C_3N_4/X ternary photocatalysts is considered, where X represents other semiconductor or noble metal. This strategy is expected to not only facilitate the charge carrier transfer at the interface of LDH and g-C_3N_4, but also improve the harvesting ability for visible light.

As shown in Fig. 4, Tonda and Jo [31] incorporated 1 wt% Ag nanoparticles into Ni-AlLDH/g-C_3H_4 composites with various weight percentages of Ni-Al-LDH (5, 10, 15, and 20 wt%, denoted as ALDHCN-5, ALDHCN-10, ALDHCN-15, and ALDHCN-20 by the authors, respectively) and studied their photocatalytic performance in degrading RhB and 4-chlorophenol (4-CP). In their study, the Ni-Al-LDH/g-C_3H_4 composites were first fabricated through hydrothermal method, and then the composites were decorated with Ag nanoparticles via a photo-reduction process to form Ni-Al-LDH/g-C_3N_4/Ag hybrids (Fig. 4a). The deposition of Ag nanoparticles on Ni-Al-LDH/g-C_3H_4 was clearly observed with TEM image (Fig. 4b). The combination of Ni-Al-LDH and g-C_3H_4 greatly increased the photocatalytic activity in degrading both RhB and 4-CP, while the incorporation of Ag nanoparticles further enhanced the photocatalytic performance (Fig. 4c and d). In the mechanism study, the photocatalytic activity of ALDHCN-15 was significantly inhibited in the presence of ammonium oxalate (AO, h^+ scavenger), benzoquinone (BZQ, $\cdot O^{2-}$ scavenger), tert-butanol (TBA, $\cdot$OH scavenger). The order of inhibiting ability was BZQ N TBA N AO (Fig. 4e). This result demonstrated that $\cdot O^{2-}$ and $\cdot$OH were the main active species that accounted for the pollutant degradation. The generation of $\cdot$OH during the photocatalytic process was further confirmed by $\cdot$OH trapping PL spectra in terephthalic acid solution (Fig. 4f). The possible photocatalytic mechanism of Ni-Al-LDH/g-C_3N_4/Ag composite was illustrated in Fig. 4g. Both Ni-Al-LDH and g-C_3N_4 could generate electron-hole pairs under visible light. Because the CB of g-C_3N_4 (-1.32 eV) is more negative than that of Ni-Al-LDH (-0.72 eV), the electrons

on the CB of g-C_3N_4 could move to the CB of Ni-Al-LDH. Similarly, the holes on the VB of Ni-AlLDH could transfer to the VB of g-C_3N_4. This facilitated the electronhole separation. The surface Ag nanoparticles on the composites were excellent electron trappers, which could transfer electrons from the CB of both Ni-Al-LDH and g-C_3N_4. Therefore, the electron-hole separation efficiency was further enhanced, contributing to the higher photocatalytic performance.
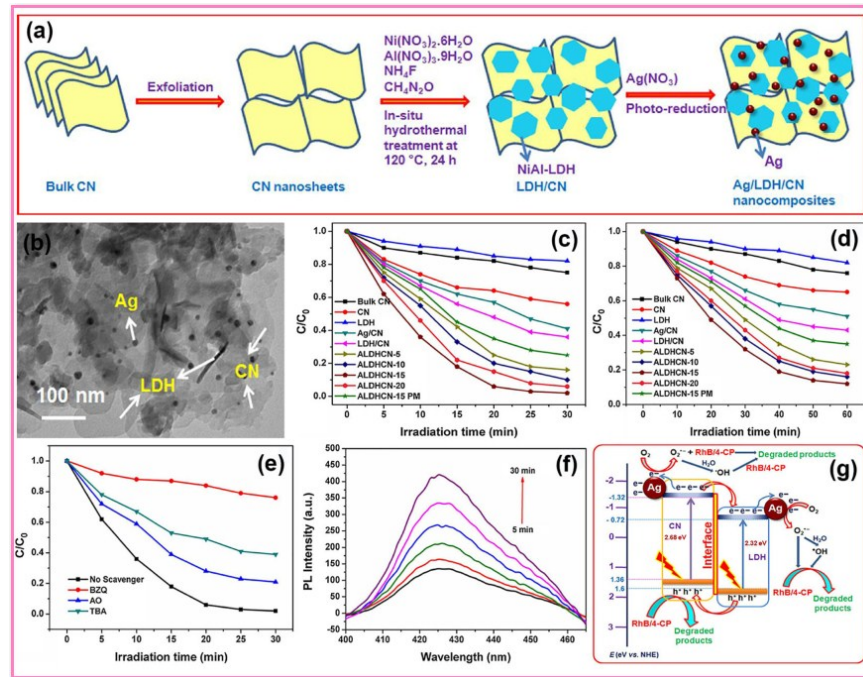

Fig. 4. Photocatalytic mechanism of single g-C_3N_4 system.

Nayak et. al [32] reported a series of heterostructure NiFe LDH/N-rGo/g-C_3N_4 (CNNG3LDH) nanocomposite were fabricated by combining calcinations-electrostatic self-assembly and hydrothermal steps as shown in Fig. 5. Among the as synthesized heterostructure, CNNG3LDH performed superior photocatalytic activities towards 95 and 72% mineralization of RhB and phenol. Furthermore, CNNG3LDH could achieve the highest photocatalytic H_2 evolution rate of 2508 µmolg-12h^{-1} and O_2 evolution rate of 1280 µmolg-12h^{-1} under visible light irradiation. The CNNG3LDH possess lowest PL intensity, reduced arc of the Nyquist plot (43.8 û) and highest photocurrent density (-0.97 mA cm^{-2}) which revealed effective charge separation for superior photocatalytic activities.

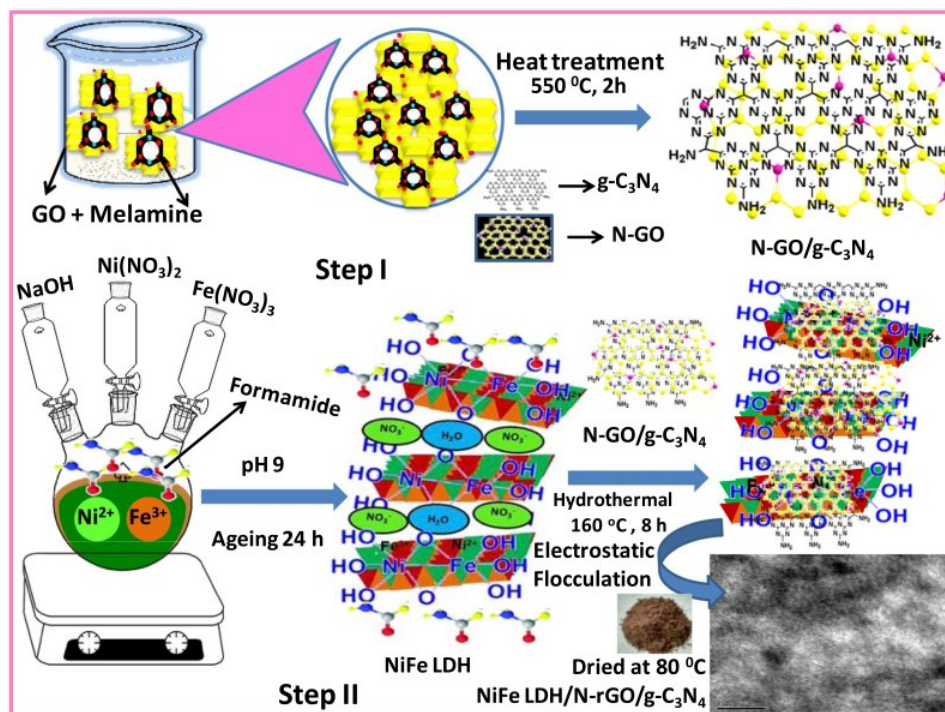**Fig. 5. Synthetic steps of heterostructure NiFe LDH/N-rGO/g-C$_3$N$_4$.**

TEM images of heterostructure CNNG3LDH nanocomposite (Fig. 6a–d) revealed that the heterostructure possesses multiple overlapping of nanosheets in which NiFe LDH and CN were electrostaticaly assembled with the surface of N-rGO framework. The tiny sized pores created on the surface of CN nanosheets by the gas released during the pyrolysis process allows for the efficient scattering of light during photocatalytic reactions. The positively charged exfoliated NiFe LDH nanosheets (Fig. 6f), was grown firmly on the edge of g-C$_3$N$_4$/N-rGO and adhere to the negatively charged N-rGO sheets through electrostatic interaction and resulted in the formation of heterostructure CNNG3LDH nanocomposite (Fig. 6a–e). The photo-degradation rate was determined by plotting C/C$_0$ vs. time (Fig. 6g) using the following Eq:

Photo-degradation rate = (C$_0$ - C/C$_0$) × 100

where C$_0$ is the initial concentration at time t=0 min C is the concentration at time 't' min. For better quantitative understanding of the reaction kinetics of the synthesized heterostructure, kinetic analysis of the degradation of RhB dye was carried out under sun light irradiation using the Langmuir–Hinshelwood model Eq. as follows:

$$\ln(C_0 /C) = k_{app} t$$

where k app is the apparent rate constant. The kinetics of the rate constant is calculated by the linear plot between ln (C$_0$/C) vs. irradiation time as shown in Fig. 6h.
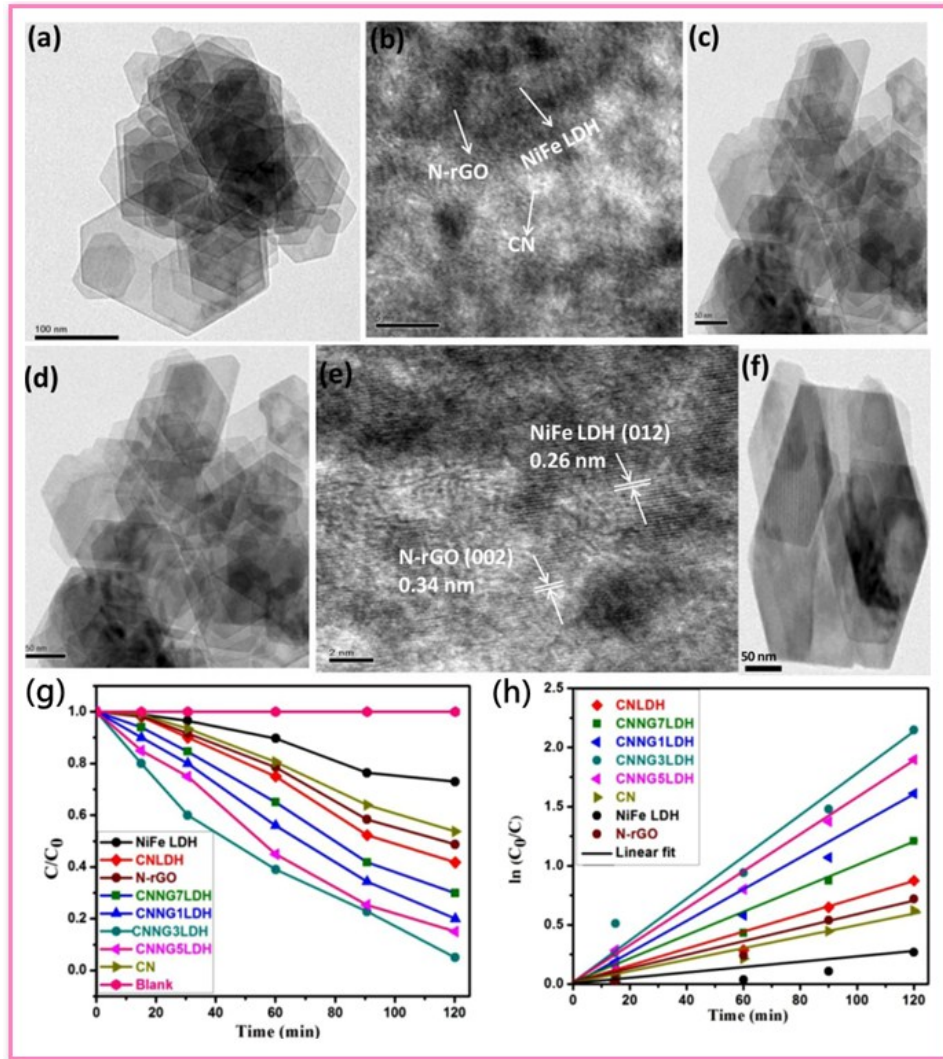
Fig. 6. (a–d) TEM images of CNNG3LDH, (e) HR-TEM images of CNNG3LDH showing lattice fringes of N-rGO and NiFe LDH, (f) TEM image of NiFe LDH, and (g) C/C0 *vs*. time plot of RhB degradation and (h) Kinetics of RhB degradation with NiFe LDH, CN, N-rGO, CNLDH and CNNGxLDH.

3.2 g-C$_3$N$_4$/2D semiconductor photocatalysts

Considering the possible synergic effect between TiO$_2$ nanosheet and g-C$_3$N$_4$ nanosheet, the novel facets coupling of g-C$_3$N$_4$ {0 0 2} and F-TiO$_2$ {0 0 1} facet hybrid was prepared by hydrothermal method without any catalysts or templates [32]. Fig. 7a–c shows the SEM images of F-TiO$_2$, g-C$_3$N$_4$ and 30%g-C$_3$N$_4$/F-TiO$_2$ hybrids. As indicated in Fig. 3a, the large amount of F-TiO$_2$ nanosheets with side length of 50–60 nm and thickness of 10–15 nm can be easily observed. The g-C$_3$N$_4$ shows the wrinkle two-dimensional structure in Fig. 7b. EDS in Fig. 7d shows the presence of F element on TiO$_2$ nanosheets.

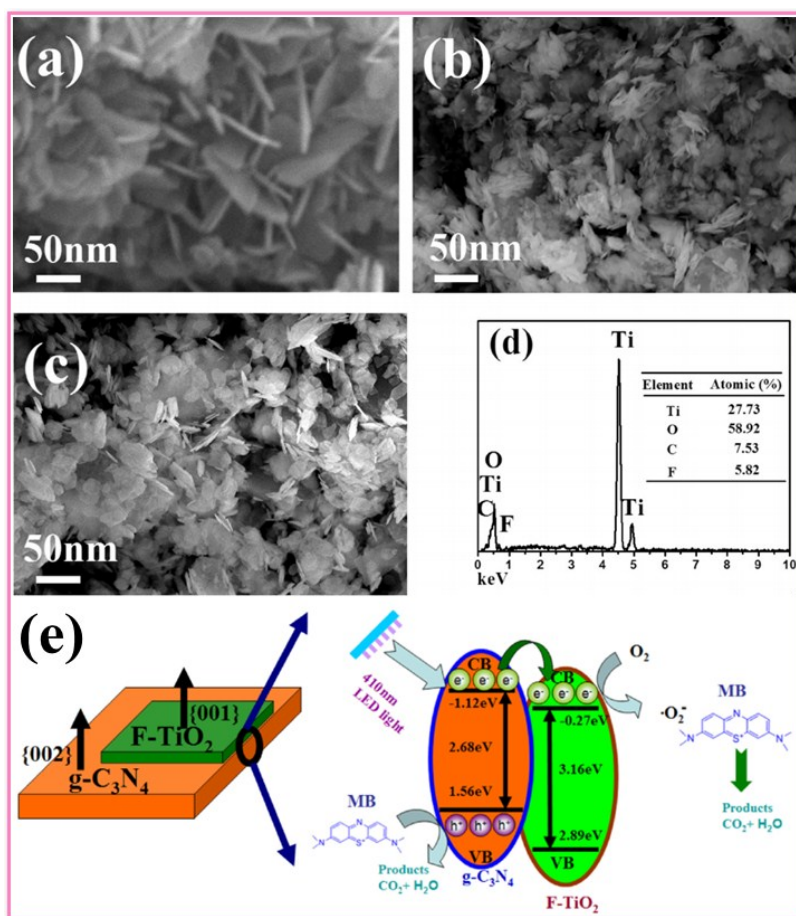Fig. 7. SEM images of (a) F-TiO$_2$, (b) g-C3N4 and (c) 30%g-C$_3$N$_4$/F-TiO$_2$ hybrids, EDS spectra of (d) F-TiO$_2$, and proposed visible LED light photodegradation mechanism of g-C$_3$N$_4$/F-TiO$_2$ hybrid photocatalyst.

Fig. 8a shows the MB adsorption on Degussa P25, F-TiO$_2$, g-C$_3$N$_4$ and g-C$_3$N$_4$/F-TiO$_2$ hybrid in the dark. F-TiO$_2$ shows the highest adsorption capacity because of its highest specific surface area. The photocatalytic activity of g-C$_3$N$_4$/F-TiO$_2$ photocatalysts was studied by degradation of MB under 410 nm LED light irradiation sources. As a comparison, MB degradation with pure TiO$_2$, Degussa P25 and no catalyst was also carried out under identical conditions. As shown in Fig. 8b, the degradation of MB in Degussa P25, TiO$_2$, 5% g-C$_3$N$_4$/F-TiO$_2$, 10%g-C$_3$N$_4$/F-TiO$_2$, 30%g-C$_3$N$_4$/F-TiO$_2$, 50%g-C$_3$N$_4$/F-TiO$_2$ and g-C$_3$N$_4$ was 15%, 34%, 59%, 71%, 89%, 61% and 42%, respectively. According to Fig. 8 a and b, the absorption of MB on all these materials is not a major factor that obviously influence their photocatalytic performance. Fig. 8c shows that there is a linear relationship between $\ln C_0/C$ and t, confirming that the photodegradation reaction is indeed pseudo-first-order. According to Fig. 8c and d shows the apparent pseudo-first-order rate constant k$_{app}$ with different catalysts. K$_{app}$ of the photodegradation of MB are 0.0027, 0.0083, 0.0166, 0.0230, 0.0374, 0.0184, 0.0096 min-1 for Degussa P25,

TiO_2, 5%g-C3N4/F-TiO_2, 10%g-C_3N_4/F-TiO_2, 30%g-C_3N_4/F-TiO_2, 50%g-C_3N_4/F-TiO_2 and g-C_3N_4, respectively. An optimal degradation performance of 89% MB was found for 30%g-C3N4/F-TiO_2, 30%g-C_3N_4/F-TiO_2 showing superior catalytic activity to commercial Degussa P25, pure TiO_2 and other g-C_3N_4/F-TiO_2 hybrids.
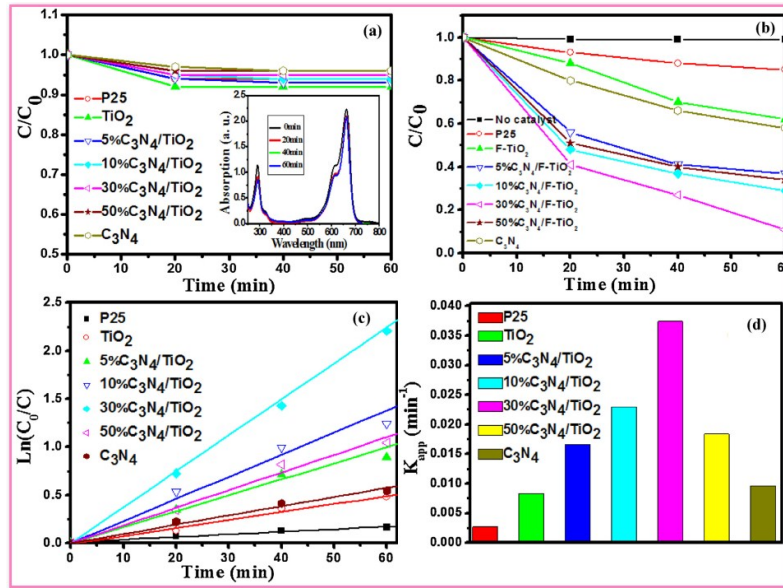

Fig. 8. (a) MB adsorption on Degussa P25, F-TiO_2, g-C_3N_4 and g-C_3N_4/F-TiO_2 hybrid in the dark (Inset: Absorption spectra of MB in the presence of 30%g-C_3N_4/F-TiO_2 composite), (b) photocatalytic degradation of MB under 410 nm LED light irradiation, (c) linear transform $ln(C_0/C)$ of the kinetic curves of MB degradation, (d) the apparent pseudo-first-order rate constant kapp with different catalysts.

Jiang et. al. reported a series of two-dimensional $CaIn_2S_4$/g-C_3N_4 heterojunction nanocomposites with intimate interfacial contact which have been synthesized by a facile two-step method [33]. Compared with pristine g-C_3N_4 and $CaIn_2S_4$, the $CaIn_2S_4$/g-C_3N_4 heterojunction nanocomposites exhibited significantly enhanced H_2 evolution and photocatalytic degradation of methyl orange (MO) activities under visible light irradiation. As shown in Fig. 9a, the g-C_3N_4 exhibits thin and irregular nanosheet structure with wrinkles, in agreement with the typical structural characteristic of graphite-like carbon nitride. In Fig. 9b, the TEM image shows the as-prepared $CaIn_2S_4$ is an irregular nanoplate with a diameter of around 20 nm. Figure 9c and d show the typical structure of the 30% $CaIn_2S_4$/g-C_3N_4 nanocomposite. The $CaIn_2S_4$ nanoplates anchor dispersedly across the g-C_3N_4 nanosheets, which form a two-dimensional heterostructure with intimate interfacial contact. The selected region marked by the red lines in Figure 9c is magnified to examine the detailed structure of the 30% $CaIn_2S_4$/g-C_3N_4 nanocomposite (Fig. 9d). As shown in Fig. 9e, the clear lattice fringes with a d-spacing of 0.278 nm, corresponding to the (400) planes of cubic phase $CaIn_2S_4$, indicating the nanoplates are $CaIn_2S_4$ with the two-dimensional structure. The morphology of the 30% $CaIn_2S_4$/g-C_3N_4 nanocomposite was further confirmed by the HAADF-STEM image (Figure 9f).

The elemental mappings (Fig. 9g) reveal that Ca, In, S, C, and N elements coexistently distributed in the 30% $CaIn_2S_4/g-C_3N_4$ nanocomposite, and the $CaIn_2S_4$ dispersed on the surface of $g-C_3N_4$ also can be confirmed by the signals intensity of different elements.

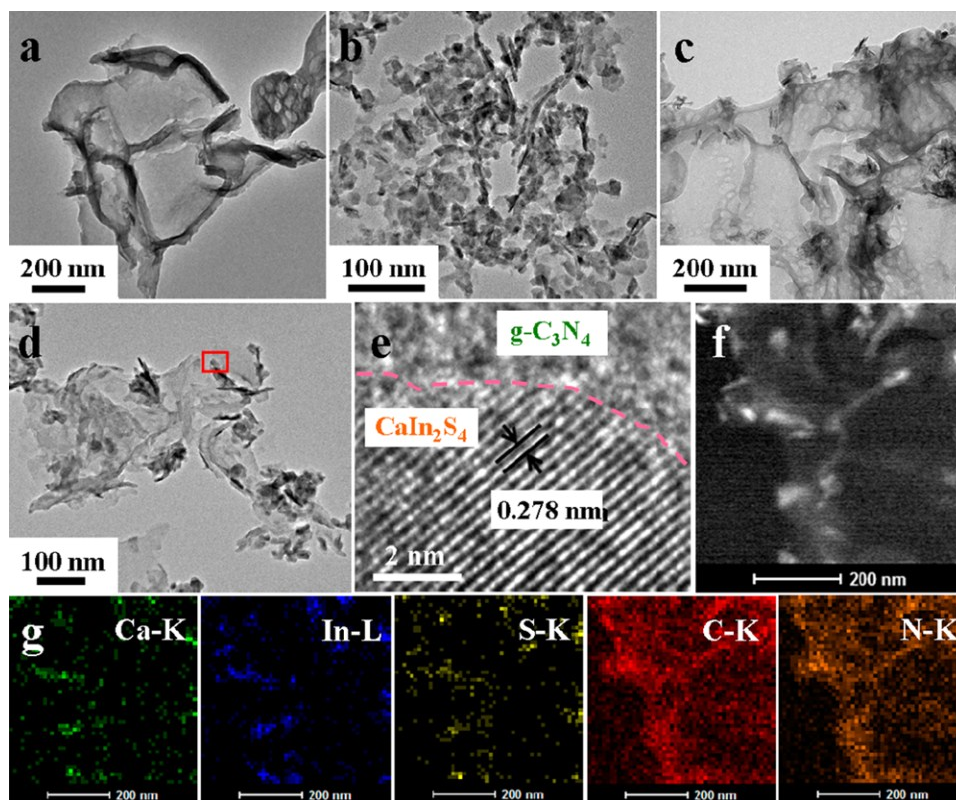**Fig. 9. TEM images of (a) $g-C_3N_4$, (b) $CaIn_2S_4$, (c, d) the 30% $CaIn_2S_4/g-C_3N_4$ heterojunction nanocomposite, the HRTEM image of the 30% $CaIn_2S_4/g-C_3N_4$ heterojunction nanocomposite (e), HAADFSTEM-EDS mapping (f) and the spatially resolved Ca, In, S, C, and N elements of the 30% $CaIn_2S_4/g-C_3N_4$ heterojunction nanocomposite (g).**

Fig. 10a shows the photocatalytic H_2 production activity of $g-C_3N_4$, $CaIn_2S_4$, and $CaIn_2S_4/g-C_3N_4$ heterojunction nanocomposites with different contents of $CaIn_2S_4$ from an aqueous solution containing 0.5 M Na_2S and 0.5 M Na_2SO_3 under UV light irradiation (triggered by 12 W UV-LEDs light). It can be seen that the H2 evolution is negligible over the pristine $g-C_3N_4$, which is consistent with the previous report [34, 35], and the in the 50% $CaIn_2S_4/g-C3N_4$ heterojunction nanocomposite is less than the pure $CaIn_2S_4$, resulting in the lower H_2 evolution rate than pristine $CaIn_2S_4$. Therefore, a suitable content of $CaIn_2S_4$ is crucial for optimizing the photocatalytic activity of $CaIn_2S_4/g-C_3N_4$ nanocomposites. As shown in Fig.10c and d, after three and five recycles, both the H_2 evolution rate and the activity of photocatalytic degradation of MO did not show a significant decrease. These results indicate that the as-prepared $CaIn_2S_4/g-C_3N_4$ heterojunctions have relatively high stabilities during photocatalytic H_2 production and degradation of MO.
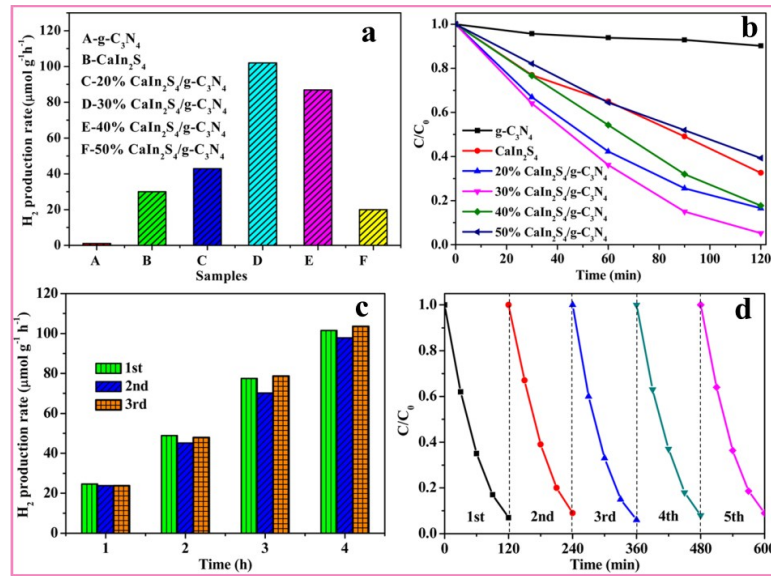
Fig. 10. (a) Comparison of the photocatalytic H₂ production activity under visible light irradiation (triggered by 12 W UV-LEDs light) and (b) photocatalytic degradation efficiency under visible light irradiation (triggered by 500 W tungsten light lamp) over g-C₃N₄, CaIn₂S₄, and CaIn₂S₄/g-C₃N₄ nanocomposites with different contents of CaIn₂S₄; (c) Stability study of photocatalytic H₂ production activity and (d) photocatalytic degradation efficiency over the 30% CaIn₂S₄/g-C₃N₄ heterojunction nanocomposite.

3.3 g-C₃N₄/nanoscale photocatalysts

Liu et.al.[36] designed g-C₃N₄@S deficient CuIn₅S₈ hollow structures (CN@VS-CIS) with improved visible-light photocatalyst activity for CO_2 reduction (as shown in Fig. 11). SiO_2 nanospheres were adopted as the templates to fabricate uniformly dispersed hollow core–shell structures with g-C₃N₄ shells. Subsequently, the growth of $CuIn_5S_8$ on the surface of hollow carbon was realized by a hydrothermal method.
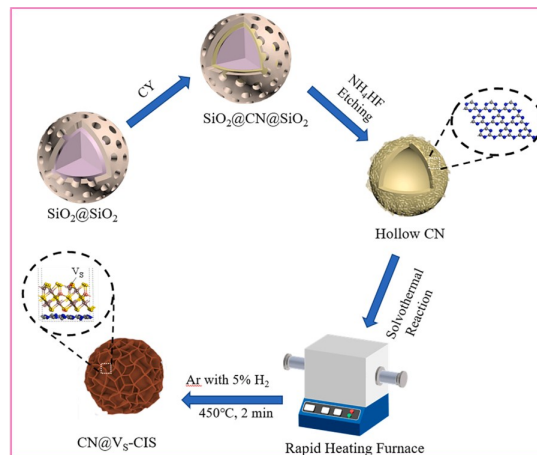

Fig. 11. Representative illustration of the assembling of CN@VS- CIS heterostructures.

This finding confirms the formation of the heterojunction between g-C_3N_4 and $CuIn_5S_8$. The elemental mapping images (Fig. 12 e-j) ascertain the coexistence of C, N, Cu, In and S in CN@34.1 wt% VS-CIS hollow photocatalysts. The S vacancy is realized by rapid heating method arrived at 450 ! in only 5 min. Vacancies could effectively trap surface-arrived charge carriers, which significantly improve charge separation efficiencies. Simultaneously, the electron-donating nature of localized electrons around defects can activate inert absorbed molecules. The specific hollow nanosphere structures can make multiple scattering light inside the cavity, shortening the distance of charge carriers. Most notably, when hollow g-C_3N_4 is loaded with 34.1 wt% $CuIn_5S_8$, it deliveries the highest produced rates of CH_4 4.8 μmol g-1h-1 and CO 1.4 μmol g-1h-1, and the catalyst capacity remains rather stable after 5 cycles. As for CN@VS-CIS with different contents, CH_4 generates since the beginning. Particularly, for the sample of CN@34.1 wt% VS-CIS heterojunction, the product of CH_4 continuously increases. After 6 h, the yield reaches a rather high 28.8 μmol g-1h-1, which is nearly over 10 times higher than hollow g-C_3N_4. Therefore, besides hollow structure engineering, the CN@VS-CIS heterojunctions and S vacancies play important roles for its high activity and selectivity.
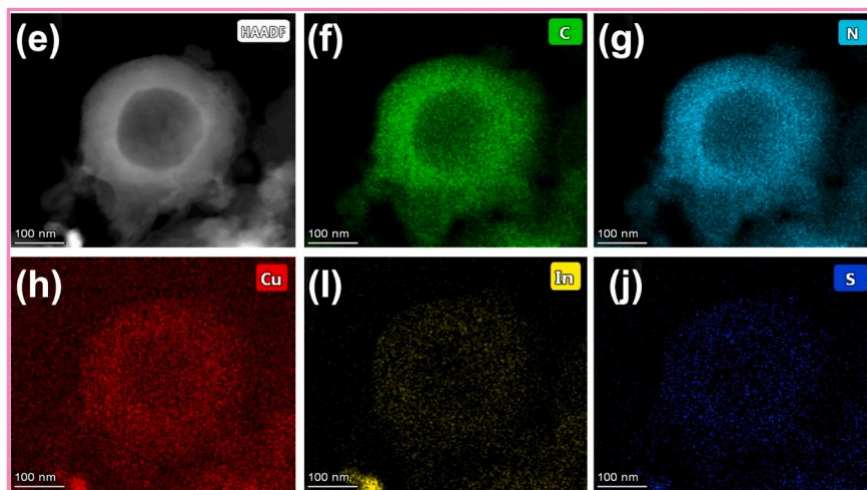

Fig. 12. EDX mapping images (the element of C, N, Cu, In, S) of CN@34.1 wt% VS-CIS heterojunction.
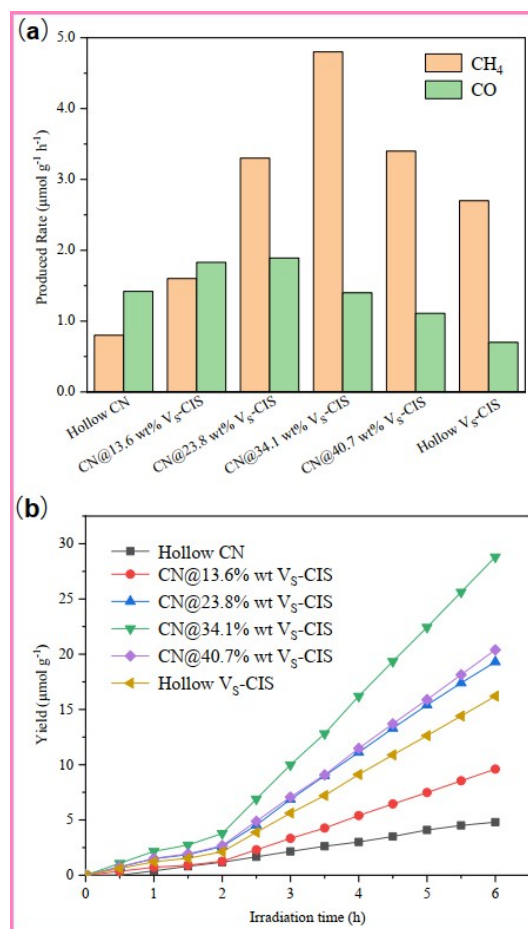
Fig. 13. (a) Photocatalytic products generation rates over hollow g-CN, CN@VSCIS heterojunction with different contents of VS- CIS nanosheets (wt 13.6%, wt 23.8%, wt 34.1% and wt 40.7%) and hollow VS-CIS nanosheets for 6 h illumination. (b) Time courses of photocatalytic CH$_4$ production of the prepared samples under visible light irradiation for 6 h.

Liu et al. demonstrated a combined deposition-precipitation method and heat treatment to produce C$_3$N$_4$/ZnO photocatalysts, for which the optimal weight ratio of C$_3$N$_4$ was 5.0 wt.% [37]. Two lattice fringes with d = 0.325 and 0.279 nm overlapped mutually (Fig. 14a and 14b), which were corresponded to the (002) plane of C$_3$N$_4$ and (100) plane of ZnO respectively, suggesting a heterostructure was formed. By contrast, the optimized removal rates for RhB and Cr^{6+} of C$_3$N$_4$/ZnO were 3 and 5 times faster than those of raw C3N4, respectively. The enhanced photoactivity was mainly owing to efficient charge separations by injecting excited e" from C$_3$N$_4$ into ZnO (Fig.14c). Several similar studies have also been explored by using mpg C$_3$N$_4$ and g-C$_3$N$_4$ nanosheets as supporters. Chen and co-workers firstly obtained mpg-C$_3$N$_4$ by a hard template method with SiO$_2$ as template agent, and then decorated ZnO NPs on it through the hydrothermal reaction (Fig. 14d) [38]. The photocurrent increased remarkably in the optimized ZnO/mpg-C$_3$N$_4$ over 3 times with ë > 420 nm light irradiating (Fig. 14e),

which resulted from the efficient separation of photogenerated e^- - h^+ pairs because of their strong synergistic effects. While, Li et al. received ALD-based g-C_3N_4@ZnO photocatalysts via a thermal atomic layer deposition method by using g-C_3N_4 nanosheets as supporters, as depicted in Fig. 14f [39]. This photocatalyst exhibited outstanding photodegradation (98.9%) and mineralization (72.8%) efficiencies for cephalexin within 60 min, and excellent photostability of g-C_3N_4@ZnO nanocomposites were also discovered.
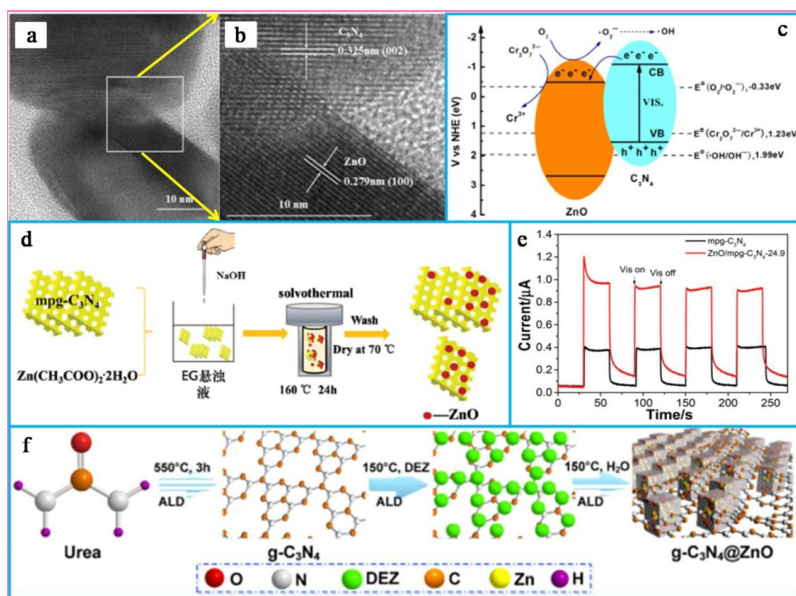

Fig. 14. (a) TEM and (b) HRTEM image of C_3N_4 (5.0 wt.%)/ZnO samples, and (c) the proposed mechanisms of charge separation and transfer process for C_3N_4/ZnO photocatalysts [37]; (d) the schematic diagram of fabrication process for ZnO doped mpg-C_3N_4 composites and (e) transient photocurrent responses of mpg-C_3N_4 and optimal ZnO/mpg-C3N4 under » e" 420 nm irradiation in 0.1 M Na_2SO_4 solutions [38]; And (f) synthesis of ALD-based g-C_3N_4@ZnO catalysts by a thermal atomic layer deposition method [39].

4. Summary

Tremendous modification strategies have been implemented to develop efficient g-C_3N_4 based photocatalysts over the past several years, which exhibit superior chemical properties and photoelectric characteristics. This review comprehensively discusses the recent advances in engineering g-C_3N_4 by fabricating heterostructures and constructing diverse morphologies for enhanced photocatalytic performance. On one hand, such heterojunctions contain g-C_3N_4/LDH, g-C_3N_4/2D semiconductor based material and many other nanoscale materials modified g-C_3N_4 composites. Several charge transfer pathways occur in these nanohybrids under visible light have also been explicated in detail. Once forming heterojunctions with unique architectures, the improved visible-light photocatalytic activity of g-C_3N_4 based catalysts is mainly derived from a well visible-light response, high chemical stability, strong redox ability and fast charge migration and separation processes.

References

1. Y. Wang, X. Wang and M. Antonietti, Angew. Chem. Int. Ed. **51** (2012) 68.

2. G. Dong, Y. Zhang, Q. Pan and J. Qiu, J. Photochem. Photobio. C **20** (2014)33.

3. X. H. Li and M. Antonietti, Chem. Soc. Rev. **42** (2013) 6593.

4. F.Y. Cheng, H. Yin, and Q.J. Xiang, Appl. Surf. Sci. **391** (2017) 432.

5. Y.X. Yang, W. Guo, Y.G. Guo, Y.H. Zhao, X. Yuan, Y.H. Guo, and J. Chen, Ceram. Soc. **45** (2017) 1024.

6. X.C. Wang, K. Maeda, X.F. Chen, K. Takanabe, K. Dmen, Y.D. Hou, X.Z. Fu, and M. Antonietti, J. Am. Chem. Soc. **135** (2009) 1680.

7. Y.C. Zhang, Q. Zhang, Q.W. Shi, Z.Y. Cai, and Z.J. Yang, Sep. Purif. Technol. **142**, 251 (2015).

8. Y.Y. Bu, Z.W. Chen, T. Xie, W.B. Li, and J.P. Ao, RSC Adv. **6** (2016) 47813.

9. X. Wang, S. Blechert, M. Antonietti, ACS Catal. **2** (2012) 1596–1606.

10. D. Zhang, G. Tan, M. Wang, B. Li, M. Dang, H. Ren, A. Xia, Mater. Res. Bull. **122** (2020) 110685.

11. W.J. Ong, L.L. Tan, Y.H. Ng, S.T. Yong, S.P. Chai, Chem. Rev. **116** (2016) 7159–7329.

12. Z. Tong, D. Yang, Z. Li, Y. Nan, F. Ding, Y. Shen, Z. Jiang, ACS Nano **11** (2017) 1103–1112.

13. Y. Song, J. Qi, J. Tian, S. Gao, F. Cui, Chem. Eng. J. **341** (2018) 547–555.

14. H. Liang, J. Wang, B. Jin, D. Li, Y. Men, Inorg. Chem. Commun. **109** (2019) 107574.

15. H. Zhao, X. Ding, B. Zhang, Y. Li, C. Wang, Sci. Bull. **62** (2017) 602–609.

16. Y. Bai, T. Chen, P. Wang, L. Wang, L. Ye, X. Shi, W. Bai, Sol. Energy Mater. Sol. Cells **157** (2016) 406–414.

17. M. Song, Y. Wu, G. Zheng, C. Du, Y. Su, Appl. Surf. Sci. **498** (2019) 143808.

18. Y. Wu, M. Song, Z. Chai, X. Wang, J. Colloid Interface Sci. **550** (2019) 64–72.

19. Y. Fu, W. Liang, J. Guo, H. Tang, S. Liu, Appl. Surf. Sci. **430** (2018) 234–242.

20. Y. Hong, C. Li, G. Zhang, Y. Meng, B. Yin, Y. Zhao, W. Shi, Chem. Eng. J. **299** (2016) 74–84.

21. Y. Zang, L. Li, X. Li, R. Lin, G. Li, Chem. Eng. J. **246** (2014) 277–286.

22. T. Ma, J. Bai, C. Li, Vacuum **145** (2017) 47–54.

23. H. Li, J. Liu, W. Hou, N. Du, R. Zhang, X. Tao, Appl. Catal., B **160**, 89 (2014).

24. M. Liu, S.J. Wei, W. C, L. Gao, X.Y. Li, L.Q. Mao, H.F. Dang, J. CHIN. CHEM. SOC **67** (2020) 246-252

25. G. Mamba, A.K. Mishra, Appl. Catal. B **198** (2016) 347–377.

26. T.S. Natarajan, K.R. Thampi, R.J. Tayade, Appl. Catal. B **227** (2018) 296–311.

27. S. C. Yan, S. B. Lv, Z. S. Li and Z. G. Zou, Dalton. Trans. **39** (2010) 1488–1491

28. Y. Hong, C. Li, G. Zhang, Y. Meng, B. Yin, Y. Zhao, W. Shi, Chem. Eng. J **299** (2016) 74–84.

29. L. Ge, C. Han, J. Liu, Y. Li, Appl. Catal. A. **409–410** (2011) 215–222.

30. W.K. Jo, S. Tonda, J. Hazard. Mater. **368** (2019) 778–87.

31. S. Tonda, W.K. Jo, Catal. Today. **315** (2018) 213–22.

32. K. Dai, L.H. Lu, C.H. Liang, Q. Liu, G.P. Zhu, Appl. Catal. B **156–157** (2014) 331–340

33. D.L. Jiang, J. Li, C.S. Xing, Z.Y. Zhang, S.C. Meng, M. ChenÿACS Appl. Mater. Interfaces. **2015**, 7, 19234-19242

34. Z.H. Chen,; Sun, P.; Fan, B.; Zhang, Z. G.; Fang, X. M. J. Phys. Chem. C 2014, **118**, 7801-7807.

35. H. Zhao, Y. M.Dong, P. P. Jiang, H. Y. Miao, G. L. Wang, J. J. Zhang, J. Mater. Chem. A **3** (2015) 7375-7381.

36. S.M. Liu, L.J. Chen, T.T.Liu, S. Cai, X.X. Zou, J.W. Jiang, Z.Y. Mei, Z.H. Gao, H.GuoÿChem. Eng. J. **424** (2021) 130325

37. W. Liu, M. Wang, C. Xu, S. Chen, Chem. Eng. J. **209** (2012) 386–393.

38. D. Chen, K. Wang, T. Ren, H. Ding, Y. Zhu, Dalton Trans. **43** (2014) 13105–13114.

39. N. Li, Y. Tian, J. Zhao, J. Zhang, W. Zuo, L. Kong, H. Cui, Chem. Eng. J. **352** (2018) 412–422.